that is expected to be the same for every merger configuration, so measurements from the different systems can be simply averaged (with appropriate noise weighting, although in practice, the constraining power from weak lensing-only measurements comes roughly equally from all of the systems).

Combining measurements of all of the colliding systems, we measure a fractional lag of dark matter relative to gas $\langle\beta\rangle = -0.04 \pm 0.07$ (68% CL). Interpreting this through our model implies that dark matter's momentum transfer cross section is $\sigma_{DM}/m = -0.25^{+0.42}_{-0.43}$ cm$^2$/g (68% CL, two-tailed) or $\sigma_{DM}/m < 0.47$ cm$^2$/g (95% CL, one-tailed) (Fig. 4). This result rules out parts of model space of hidden-sector dark matter models [e.g., (12, 13, 15, 16)] that predict $\sigma_{DM}/m \approx 0.6$ cm$^2$/g on cluster scales through a long-range force. The control test found $\langle\beta_\perp\rangle \equiv \langle\delta_{DI}/\delta_{SG}\rangle = -0.06 \pm 0.07$ (68% CL) ($\beta_\perp$, fractional displacement perpendicular to the vector connecting the galaxies and the gas), consistent with zero as expected. This inherently statistical technique can be readily expanded to incorporate much larger samples from future all-sky surveys. Equivalent measurements of mass loss during collisions could also test dark sector models with isotropic scattering. Combining observations, these astrophysically large particle colliders have potential to measure dark matter's full differential scattering cross section.

## REFERENCES AND NOTES

1. M. Davis, G. Efstathiou, C. S. Frenk, S. D. M. White, *Astrophys. J.* **292**, 371–394 (1985).
2. J. Dubinski, R. G. Carlberg, *Astrophys. J.* **378**, 496–503 (1991).
3. A. Klypin, A. V. Kravtsov, O. Valenzuela, F. Prada, *Astrophys. J.* **522**, 82–92 (1999).
4. B. Moore et al., *Astrophys. J.* **524**, L19–L22 (1999).
5. M. Boylan-Kolchin, J. S. Bullock, M. Kaplinghat, *Mon. Not. R. Astron. Soc.* **415**, L40–L44 (2011).
6. A. Pontzen, F. Governato, *Nature* **506**, 171–178 (2014).
7. J. M. Bardeen, J. R. Bond, N. Kaiser, A. S. Szalay, *Astrophys. J.* **304**, 15–61 (1986).
8. D. N. Spergel, P. J. Steinhardt, *Phys. Rev. Lett.* **84**, 3760–3763 (2000).
9. M. Rocha et al., *Mon. Not. R. Astron. Soc.* **430**, 81–104 (2013).
10. J. Zavala, M. Vogelsberger, M. G. Walker, *Mon. Not. R. Astron. Soc.* **431**, L20–L24 (2013).
11. F. Kahlhoefer, K. Schmidt-Hoberg, M. T. Frandsen, S. Sarkar, *Mon. Not. R. Astron. Soc.* **437**, 2865–2881 (2014).
12. R. Foot, *Int. J. Mod. Phys. A* **29**, 1430013 (2014).
13. K. K. Boddy, J. L. Feng, M. Kaplinghat, T. M. P. Tait, *Phys. Rev. D Part. Fields Gravit. Cosmol.* **89**, 115017 (2014).
14. Y. Hochberg, E. Kuflik, T. Volansky, J. G. Wacker, *Phys. Rev. Lett.* **113**, 171301 (2014).
15. J. M. Cline, Z. Liu, G. D. Moore, W. Xue, *Phys. Rev. D* **90**, 015023 (2014).
16. S. Tulin, H.-B. Yu, K. M. Zurek, *Phys. Rev. Lett.* **110**, 111301 (2013).
17. D. S. Akerib et al., *Phys. Rev. Lett.* **112**, 091303 (2014).
18. S. W. Randall, M. Markevitch, D. Clowe, A. H. Gonzalez, M. Bradac, *Astrophys. J.* **679**, 1173–1180 (2008).
19. M. Markevitch et al., *Astrophys. J.* **606**, 819–824 (2004).
20. D. Eckert et al., *Astron. Astrophys.* **570**, A119 (2014).
21. M. Bartelmann, P. Schneider, *Phys. Rep.* **340**, 291–472 (2001).
22. D. Clowe, A. Gonzalez, M. Markevitch, *Astrophys. J.* **604**, 596–603 (2004).
23. L. L. R. Williams, P. Saha, *Mon. Not. R. Astron. Soc.* **415**, 448–460 (2011).
24. D. Harvey et al., *Mon. Not. R. Astron. Soc.* **433**, 1517–1528 (2013).
25. F. Gastaldello et al., *Mon. Not. R. Astron. Soc.* **442**, L76–L80 (2014).
26. R. Massey, T. Kitching, D. Nagai, *Mon. Not. R. Astron. Soc.* **413**, 1709–1716 (2011).
27. J. G. Fernández-Trincado, J. E. Forero-Romero, G. Foex, T. Verdugo, V. Motta, *Astrophys. J.* **787**, L34 (2014).
28. D. Harvey et al., *Mon. Not. R. Astron. Soc.* **441**, 404–416 (2014).
29. http://archive.stsci.edu/hst/.
30. http://cxc.harvard.edu/cda/.
31. D. Clowe et al., *Astrophys. J.* **648**, L109–L113 (2006).
32. S. Giodini et al., *Astrophys. J.* **703**, 982–993 (2009).
33. P. A. R. Ade et al., Planck Collaboration, *Astron. Astrophys.* **571**, A16 (2014).

## NEURODEVELOPMENT

# Human-specific gene *ARHGAP11B* promotes basal progenitor amplification and neocortex expansion

**Marta Florio,[1] Mareike Albert,[1]\* Elena Taverna,[1]\* Takashi Namba,[1]\* Holger Brandl,[1] Eric Lewitus,[1]† Christiane Haffner,[1] Alex Sykes,[1] Fong Kuan Wong,[1] Jula Peters,[1] Elaine Guhr,[1] Sylvia Klemroth,[2] Kay Prüfer,[3] Janet Kelso,[3] Ronald Naumann,[1] Ina Nüsslein,[1] Andreas Dahl,[2] Robert Lachmann,[4] Svante Pääbo,[3] Wieland B. Huttner[1]‡**

Evolutionary expansion of the human neocortex reflects increased amplification of basal progenitors in the subventricular zone, producing more neurons during fetal corticogenesis. In this work, we analyze the transcriptomes of distinct progenitor subpopulations isolated by a cell polarity–based approach from developing mouse and human neocortex. We identify 56 genes preferentially expressed in human apical and basal radial glia that lack mouse orthologs. Among these, *ARHGAP11B* has the highest degree of radial glia–specific expression. *ARHGAP11B* arose from partial duplication of *ARHGAP11A* (which encodes a Rho guanosine triphosphatase–activating protein) on the human lineage after separation from the chimpanzee lineage. Expression of *ARHGAP11B* in embryonic mouse neocortex promotes basal progenitor generation and self-renewal and can increase cortical plate area and induce gyrification. Hence, *ARHGAP11B* may have contributed to evolutionary expansion of human neocortex.

Neocortex expansion is a hallmark of primate (especially human) evolution (1, 2). The increased number of neurons generated during human cortical development results from increased proliferation of neural stem and progenitor cells (NPCs) (3–8). Three classes of cortical NPCs can be distinguished cell biologically: (i) apical progenitors, which undergo mitosis at the ventricular side of the ventricular zone (VZ)—i.e., apical radial glia (aRG) and apical intermediate progenitors; (ii) basal progenitors, which lack ventricular contact and undergo mitosis in the subventricular zone (SVZ)—i.e., basal (outer) radial glia (bRG) and basal intermediate progenitors (bIPs); and (iii) subapical progenitors, which undergo mitosis in the SVZ or basal VZ and retain ventricular contact (9).

Cortical expansion has been linked to increased generation of basal progenitors from aRG and their greater and prolonged proliferation, resulting in enlargement of the SVZ (3–7, 10, 11). Toward identifying the molecular basis of these processes, genome-wide transcriptome analyses of VZ and SVZ carried out in rodents (12, 13) and primates (14), including humans (13, 15), have provided insight. Further clues have come from transcriptome analyses of mouse NPC subpopulations (16) and retrospectively identified mouse and human NPC types (17–19). However, a rate-limiting step in understanding cortical expansion has been the lack of transcriptome analyses

[1]Max Planck Institute of Molecular Cell Biology and Genetics (MPI-CBG), Pfotenhauerstraße 108, D-01307 Dresden, Germany. [2]Technische Universität Dresden, Center for Regenerative Therapies Dresden, Fetscherstraße 105, D-01307 Dresden, Germany. [3]Max Planck Institute for Evolutionary Anthropology (MPI-EVA), Deutscher Platz 6, D-04103 Leipzig, Germany. [4]Technische Universität Dresden, Universitätsklinikum Carl Gustav Carus, Klinik und Poliklinik für Frauenheilkunde und Geburtshilfe, Fetscherstraße 74, D-01307 Dresden, Germany.
*These authors contributed equally to this work. †Present address: Départment de Biologie, École Normale Supérieure, 46 Rue d'Ulm, 75005 Paris, France. ‡Corresponding author. E-mail: huttner@mpi-cbg.de

of human NPC subpopulations (in particular, of bRG) thought to have a key role in this process (3–7).

We therefore sought to isolate specific NPC types from fetal human neocortex and compare them with those from embryonic mouse neocor-

tex. To this end, we exploited the differential apical-basal cell polarity of radial glia (9, 20) (Fig. 1). Radial glia contacting the basal lamina
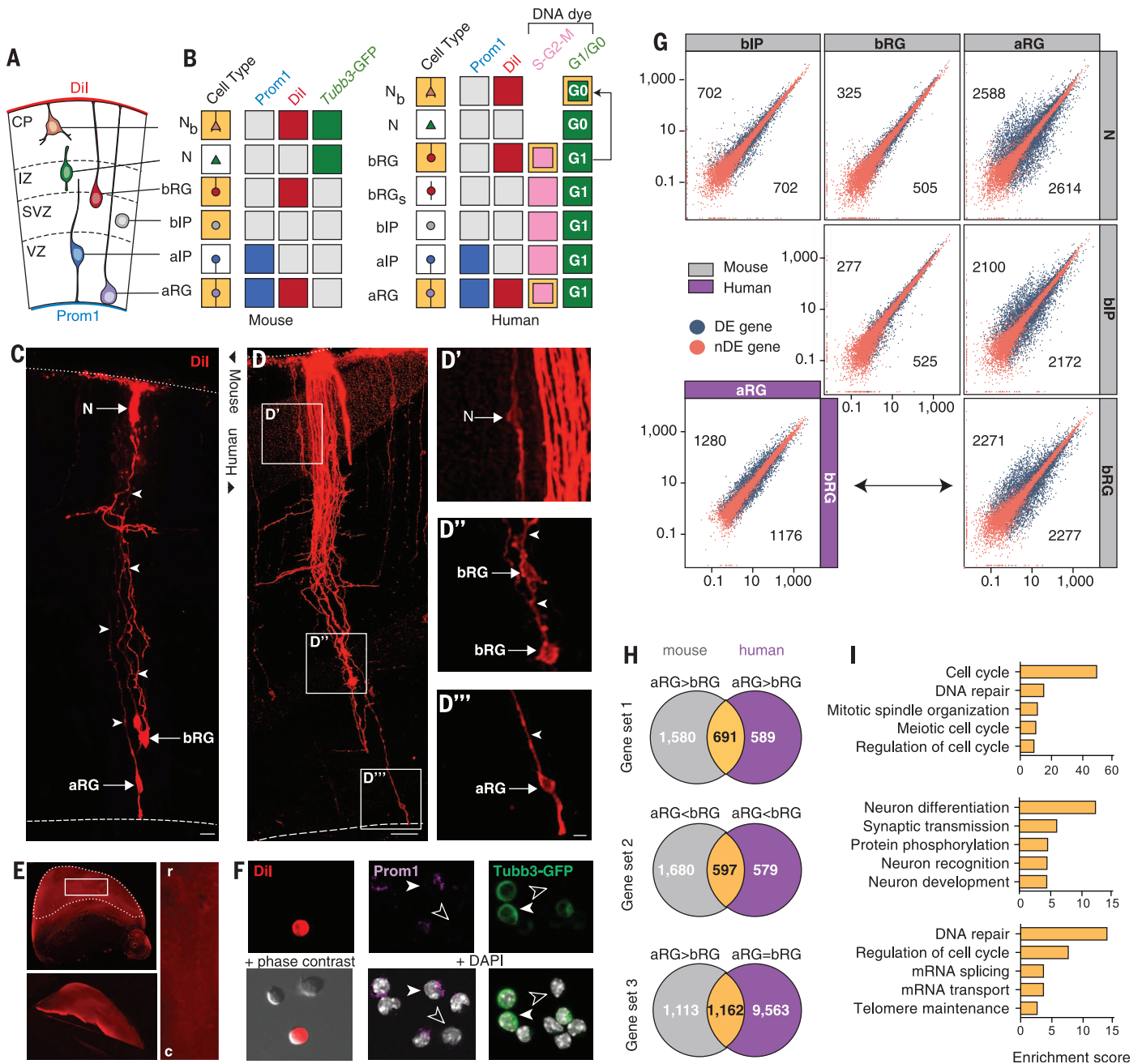


**Fig. 1. Isolation of distinct NPC types from mouse and human neocortex and comparison of their transcriptomes.** (**A**) NPC types labeled via their apical surface (Prom1) and/or basal lamina contact (DiI). N and Nb, neurons without and with basal contact, respectively; CP, cortical plate; IZ, intermediate zone. (**B**) Cell types isolated (yellow) from embryonic Tubb3-GFP mouse (left) and fetal human (right) neocortex based on the absence or presence of apical Prom1, basal DiI, neuronal Tubb3-GFP, $G_1/G_0$, and/or $S$-$G_2$-M. Human bRG with basal contact in $G_1$ are present in the Nb fraction (arrow). bRGs, secondary bRG lacking basal contact. (**C** to **D'''**) Sparse DiI labeling of E14.5 mouse (C) and 13 weeks postconception (wpc) human (D to D''') neocortex from basal lamina (dotted lines). Arrows, cell body; solid arrowheads, basal process; dashed lines, ventricular surface. DiI labeling is confined to aRG, bRG, and Nb. Scale bars, 20 μm. (**E**) Comprehensive basal DiI labeling of E14.5 Tubb3-GFP mouse

hemisphere. r, rostral; c, caudal. The bottom left image shows dissected neocortex. (**F**) Dissociated DiI-labeled, Prom1 surface–labeled and Tubb3-GFP+ cells from E14.5 Tubb3-GFP mouse neocortex. Solid and open arrowheads respectively indicate representative cells positive and negative for a given marker. (**G**) DESeq scatter plots showing pairwise comparisons of expression (FPKM) of protein-encoding genes between E14.5 mouse aRG, bRG, bIPs, and neurons (N) (gray; 12,897 genes in total) and between 13 wpc human aRG and bRG (purple; 14,302 genes in total). DE, differentially expressed (numbers); nDE, nondifferentially expressed. (**H**) Venn diagrams showing numbers of genes with indicated expression pattern in mouse and/or human aRG and bRG. (**I**) The five top-scoring clusters of significantly enriched ($P < 0.05$) GO terms (category: biological process) associated with the genes expressed in both mouse and human aRG and bRG with the indicated patterns [yellow in (B)].

via a basal process were labeled (along with basal lamina–contacting neurons) by basal application of the fluorescent membrane dye DiI (Fig. 1 and fig. S1) (see also supplementary materials and methods). This was followed by hemisphere culture to allow DiI to diffuse to the cell body of both bRG and aRG (Fig. 1 and fig. S1). NPCs that exhibited ventricular contact were labeled, after preparation of a cell suspension (Fig. 1 and fig. S1), by immunofluorescence for the apical plasma membrane marker prominin-1 (Prom1) (Fig. 1). To isolate neurons, we either used transgenic *Tubb3*–green fluorescent protein (GFP) mouse embryos (21) (Fig. 1) or, for fetal human neocortex, performed vital DNA staining of the cell suspension with a fluorescent dye to distinguish neurons ($G_0$) from NPCs (S-$G_2$-M) on the basis of their different DNA content (Fig. 1).

With these markers, we used fluorescence-activated cell sorting to isolate the following cell populations from embryonic mouse neocortex: aRG (DiI+, Prom1+, *Tubb3*-GFP−), bRG (DiI+, Prom1−, *Tubb3*-GFP−), neurons with basal lamina contact (DiI+, *Tubb3*-GFP+, Prom1−), and bIPs (DiI−, Prom1−, *Tubb3*-GFP−) (Fig. 1). Using the same DiI+/Prom1± combination, we isolated aRG and bRG in S-$G_2$-M and neurons from fetal human neocortex (Fig. 1). The authenticity of the aRG, bRG, bIP, and neuron fractions was validated by quantitative polymerase chain reaction (qPCR) analyses of appropriate markers (figs. S2 and S3).

After RNA sequencing of each cell fraction (fig. S4), differential gene expression analysis indicated that in mice, bRG are very similar to bIPs and neurons but are distinct from aRG (Fig. 1 and fig. S5). In contrast, in humans, fewer genes were differently expressed between bRG and aRG (Fig. 2 and fig. S6). Hierarchical clustering corroborated these findings (fig. S7). Further evidence showing that bRG and aRG are distinct in mice but similar in humans was obtained by (i) transcriptome analyses, including comparison of proliferative (*Tis21*-GFP−) versus differentiative (*Tis21*-GFP+) mouse aRG (fig. S8), and (ii) quantitation of mRNA versus protein of the transcription factor *Eomes*/Tbr2 (figs. S3, S8, and S9).

We therefore searched for functional clues in the set of genes that have similar expression levels in human bRG and aRG but are down-regulated in mouse bRG compared with aRG (Fig. 1). The five clusters of gene ontology (GO) terms most enriched among these genes included DNA repair and telomere maintenance (Fig. 2C). This supports (i) the emerging concept (16, 22) that proliferative NPCs invest more in DNA repair than neurogenic NPCs and (ii) the stem cell character of aRG and bRG in humans but only of aRG in mice (fig. S6). Conversely, the five GO term clusters most enriched among genes more highly expressed in both mouse and human bRG compared with aRG carried a strong neuronal differentiation signature (Fig. 1), consistent with bRG being neurogenic in both rodents and primates (5, 6, 23, 24).

Next we searched for genes specifically expressed in human aRG and bRG, starting with two separate sets of differentially expressed human genes: (i) aRG>bRG>neurons (190 genes) and (ii) bRG≥aRG>neurons (394 genes) (Fig. 2 and tables S1 and S2). We then eliminated genes that had mouse orthologs that were expressed in mouse cortical NPCs or cortical germinal zones (13), and then genes with overt [fragments per



**Fig. 2. Searching for genes specifically expressed in human radial glia reveals the hominin-specific gene *ARHGAP11B*.** (**A** and **B**) Stepwise addition of exclusion parameters to the data sets of human genes with aRG>bRG>N (neuron) (A) and bRG≥aRG>N (B) expression at 13 wpc. GZs, germinal zones; CP, cortical plate. In (B), red color indicates that only one of the 56 human-specific, bRG≥aRG−enriched genes exhibits FPKM values bRG/N ≥ 10: *ARHGAP11B*. RG, radial glia. (**C** and **D**) The five most significantly enriched GO terms associated with the 13 aRG>bRG−enriched [(A), yellow] and 207 bRG ≥ aRG−enriched [(B), yellow] human genes with mouse orthologs. (**E**) Heat map showing relative expression levels in 13 wpc human aRG, bRG, and neurons (N) of the four Rho-related genes found in the 207 bRG≥aRG−enriched human genes with mouse orthologs [(B), yellow]. (**F** to **H**) *ARHGAP11A* (F) and *ARHGAP11B* (G) mRNA levels in 13 wpc human aRG, bRG, and neurons, and qPCR of retrospectively identified 12 wpc human apical progenitors (AP), basal progenitors (BP), and neurons. Error bars in (F) and (G) indicate SD; horizontal bars in (H) denote mean. (**I**) Phylogenetic tree showing duplication of *ARHGAP11B* (red) from *ARHGAP11A* (green). (**J**) Domain structure of ARHGAP11A, truncated ARHGAP11A versions, and ARHGAP11B. Red, GAP domain; green, unique sequence in ARHGAP11B. (**K** and **L**) Immunoblots showing Rho-GAP activity of myc-tagged ARHGAP11A, truncated ARHGAP11A versions, and ARHGAP11B, as revealed by dephosphorylation of myosin phosphatase target protein 1 (MYPT1-pT853). In (K), the arrow denotes ARHGAP11B, and the arrowhead indicates ARHGAP11A$_{1-250}$.
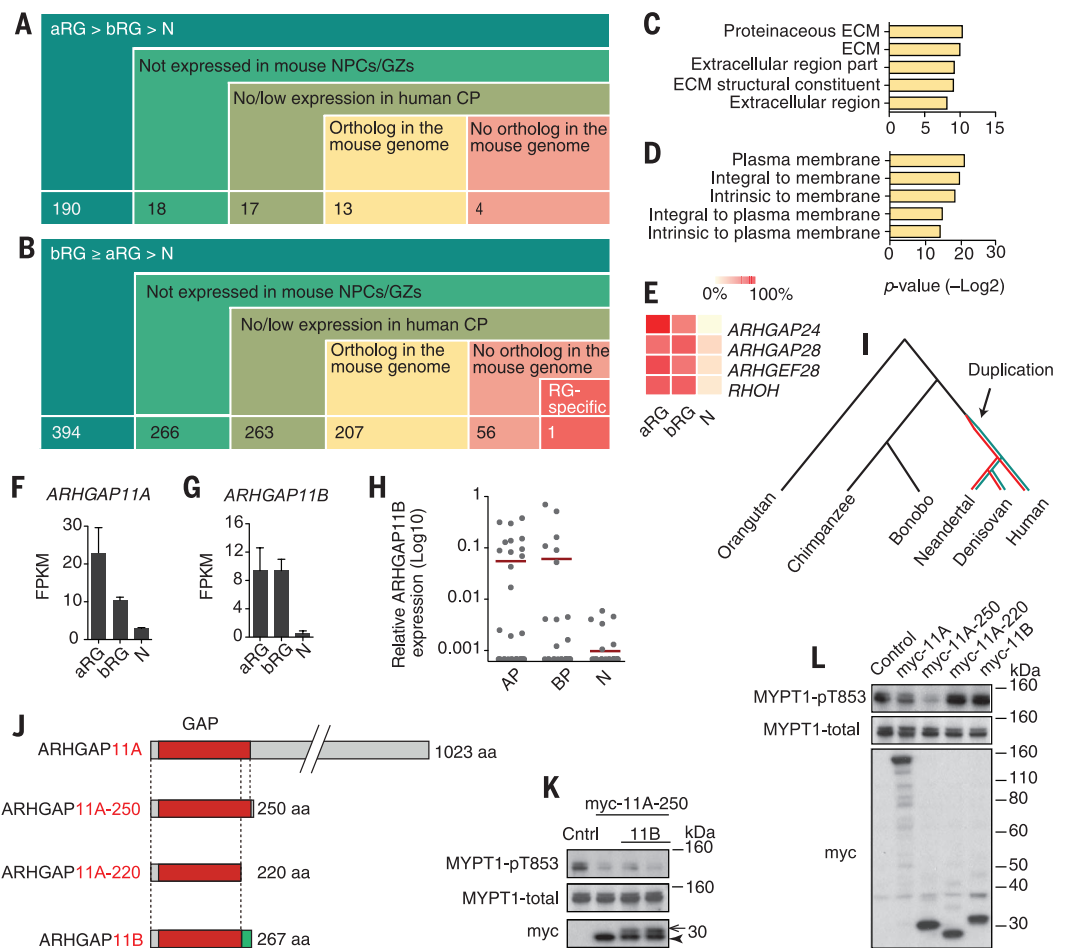
kilobase per million (FPKM) ≥ 5] expression in the human cortical plate (13). This reduced the number of human genes to 17 in the aRG>bRG>neurons gene set and to 263 in the bRG≥aRG>neurons gene set (Fig. 2). Each of these gene subsets was split into two groups: (i) human genes with orthologs in the mouse genome (which, however, are not expressed in mouse

NPCs and germinal zones) and (ii) human genes without orthologs in the mouse genome.

The five most enriched GO terms associated with the 13 human genes with mouse orthologs identified in the aRG>bRG>neurons gene set point to a role of extracellular matrix (ECM), and the GO terms associated with the 207 human genes with mouse orthologs identified in

the bRG≥aRG>neurons gene set point to a role of cell surface receptors (Fig. 2). These findings provide support for and extend the concept that endogenous production of ECM components and expression of ECM receptors by human aRG and bRG contribute to their greater proliferative potential when compared with that of mice (6, 13, 16).
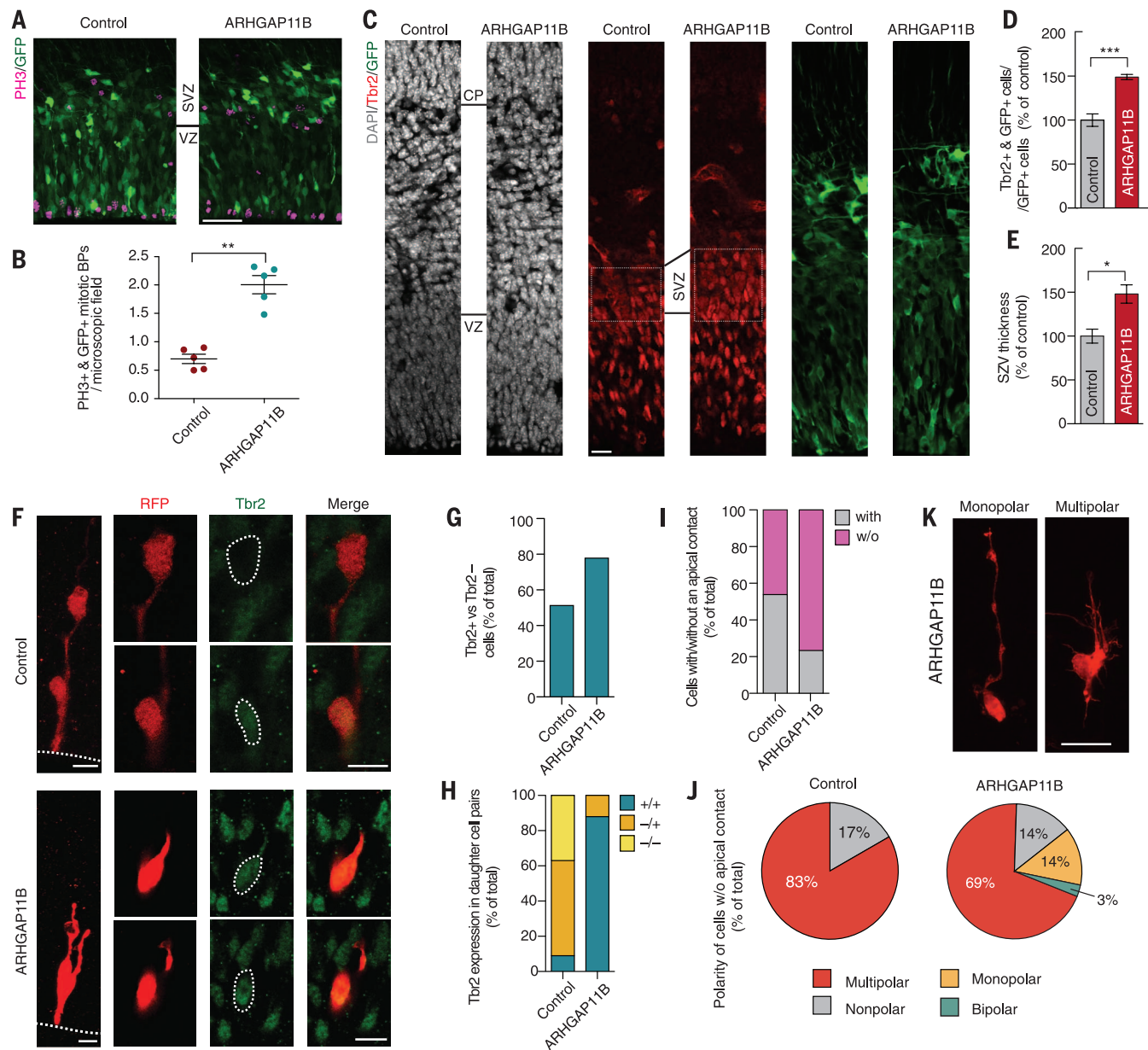


**Fig. 3. *ARHGAP11B* expression in mouse aRG increases their symmetric differentiative division, basal progenitors abundance, and SVZ thickness.** (**A** to **E**) Control and *ARHGAP11B* in utero electroporation of E13.5 mouse neocortex, followed by analysis at E14.5. (A) GFP and phosphohistone H3 (PH3) immunofluorescence. Scale bar, 50 μm. (B) Quantification of mitotic, PH3$^+$, and GFP$^+$ basal progenitors. Dots represent independent experiments; bars denote SD. **$P < 0.01$. (C) 4′,6-diamidino-2-phenylindole (DAPI) staining and Tbr2 and GFP immunofluorescence. Scale bar, 20 μm. (D) Quantification of Tbr2$^+$ and GFP$^+$ basal progenitors. Error bars indicate SD. ***$P < 0.001$. (E) Quantification of SVZ thickness relative to cortical wall. Error bars represent SEM. *$P < 0.05$. (**F** to **K**) Control and *ARHGAP11B* mRNA

microinjection into aRG in E14.5 mouse neocortex slice culture, followed by red fluorescent protein (RFP) and Tbr2 immunofluorescence after 24 hours and 48 hours. (F) Examples of asymmetric Tbr2$^-$/Tbr2$^+$ (top) and symmetric Tbr2$^+$/Tbr2$^+$ (bottom) RFP$^+$ daughter cell pairs upon control and *ARHGAP11B* microinjection, respectively. Dotted lines, ventricular surface. Scale bars, 10 μm. (G) Quantification of Tbr2$^+$ and RFP$^+$ daughter cells. (H) Quantification of Tbr2$^-$/Tbr2$^-$, Tbr2$^-$/Tbr2$^+$, and Tbr2$^+$/Tbr2$^+$ RFP$^+$ daughter cell pairs. (I) Quantification of RFP$^+$ daughter cells with and without (w/o) apical contact after 48 hours. (J) Polarity of RFP$^+$ daughter cells without apical contact. (K) Examples of monopolar and multipolar RFP$^+$ daughter cells. Scale bar, 20 μm.

We then focused our attention on the 56 human genes without mouse orthologs in the human bRG≥aRG>neurons gene set, as these were prime candidates to include human-specific genes underlying bRG expansion. As bRG in G₁ were co-isolated along with neurons from fetal human neocortex by the protocol used ($N_b$ fraction in Fig. 1), albeit at relatively low abundance (<20% of cells, as determined by Ki67 FPKM values), we concentrated on genes with FPKM values that were ≥10 times higher in bRG than in neurons to identify human genes that are truly specific for radial glia. Only one gene fulfilled this criterion: *ARHGAP11B*.

*ARHGAP11B* mRNA levels were found to be equally high in human aRG and bRG—as previously observed for human VZ, inner SVZ, and outer SVZ (*13*)—but virtually undetectable in human cortical neurons and cortical plate (Fig. 2). Single-cell qPCR of retrospectively identified human apical progenitors, basal progenitors, and neurons corroborated this finding (Fig. 2). A similar distribution across human cortical cell types (Fig. 2) and germinal zones (*13*) was ob-

served for the mRNA of *ARHGAP11A*, the paralog of *ARHGAP11B*.

*ARHGAP11B* arose on the human evolutionary lineage after the divergence from the chimpanzee lineage by partial duplication of *ARHGAP11A* (*25, 26*), which is found throughout the animal kingdom and encodes a Rho guanosine triphosphatase–activating protein (RhoGAP) (*27, 28*). *ARHGAP11B* exists not only in present-day humans but also in Neandertals and Denisovans (*26, 29–31*) (Fig. 2). ARHGAP11B contains 267 amino acids and is a truncated version of ARHGAP11A, comprising most of the GAP-domain (until Lys²²⁰) followed by a unique C-terminal sequence but lacking the C-terminal 756 amino acids of ARHGAP11A (Fig. 2 and fig. S10).

In contrast to full-length ARHGAP11A and ARHGAP11A₁₋₂₅₀, ARHGAP11B (like ARHGAP11A₁₋₂₂₀) did not exhibit RhoGAP activity in a RhoA/Rho-kinase–based cell transfection assay (Fig. 2). This indicates that the C-terminal 47 amino acids of ARHGAP11B (after Lys²²⁰) not only constitute a unique sequence, resulting from a frameshift-

ing deletion (fig. S10), but also are functionally distinct from their counterpart in ARHGAP11A. In the present assay, coexpression of ARHGAP11B along with ARHGAP11A did not inhibit the latter's RhoGAP activity (Fig. 2).

The 207 human genes with mouse orthologs in the bRG≥aRG>neurons gene set included four additional genes related to Rho signaling: *ARHGAP24*, *ARHGAP28*, *ARHGEF28*, and *RHOH* (Fig. 2). This suggests a role for Rho proteins in human radial glia.

To explore the function of ARHGAP11B in corticogenesis, *ARHGAP11B* was expressed in mouse neocortex by in utero electroporation on E13.5 (embryonic day 13.5). This increased basal but not apical mitoses and Tbr2⁺ basal progenitors at E14.5, with a similar proportion [≈30% (*16*)] of Pax6⁺ basal progenitors as in control (fig. S11). It also resulted in thickening of the SVZ (Fig. 3). In contrast, overexpression of *ARHGAP11A* did not increase basal progenitors (fig. S12).

To further dissect the effects of ARHGAP11B, we microinjected (*32*) *ARHGAP11B* mRNA into single aRG in organotypic slice culture of E14.5 mouse neocortex. After 24 hours, the same proportion of aRG progeny was identifiable as daughter cell pairs upon control versus *ARHGAP11B* microinjection (fig. S13), indicating that ARHGAP11B did not affect aRG division as such. A greater percentage of aRG progeny showed Tbr2 immunoreactivity upon *ARHGAP11B* microinjection compared with control (Fig. 3), suggesting that ARHGAP11B promoted basal progenitor generation from aRG.

Analysis of daughter cell pairs of microinjected aRG showed that in the control, the vast majority of daughter cells were either both Tbr2⁻ or one daughter cell was Tbr2⁻ whereas the other was Tbr2⁺ (Fig. 3). In contrast, upon *ARHGAP11B* mRNA microinjection, almost all daughter cell pairs observed were Tbr2⁺ (Fig. 3). We conclude that ARHGAP11B induces aRG to switch from symmetric-proliferative and asymmetric-differentiative to symmetric-differentiative divisions yielding two basal progenitors, thereby increasing their generation.

Analysis of the loss of ventricular contact of the aRG progeny corroborated this conclusion. Whereas approximately half of the progeny of control-microinjected aRG still retained ventricular contact after 48 hours of culture, nearly 80% of the progeny of *ARHGAP11B*-microinjected aRG had lost ventricular contact (Fig. 3), indicating that ARHGAP11B increases delamination. Moreover, ARHGAP11B induced the appearance of bRG-like morphology in, and a more basal localization of, the delaminated progeny (Fig. 3 and fig. S13).

*ARHGAP11B* mRNA microinjection resulted in increased clone size of the aRG progeny (Fig. 4). Consistent with this finding, *ARHGAP11B* electroporation increased the proportion of cycling cells in the SVZ (Fig. 4). Together, this shows that ARHGAP11B promotes basal progenitor self-amplification.

Finally, in half of the cases analyzed, *ARHGAP11B* expression in the normally smooth (lissencephalic) mouse neocortex, induced at E13.5, resulted
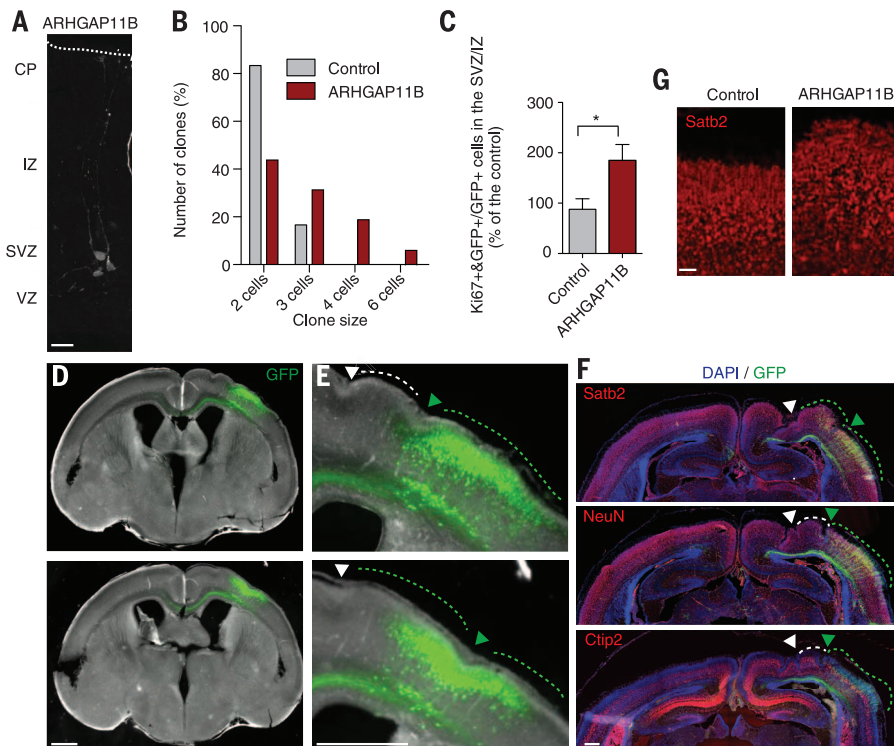


**Fig. 4.** *ARHGAP11B* expression in mouse neocortex increases basal progenitor proliferation and can induce cortical folding. (A and B) Control and *ARHGAP11B* mRNA microinjection into aRG in E14.5 mouse neocortex slice culture, followed by RFP immunofluorescence after 48 hours. (A) RFP fluorescence. Scale bar, 20 μm. (B) Quantification of daughter cell clones. (C) Control and *ARHGAP11B* in utero electroporation of E13.5 mouse neocortex, followed by quantification of Ki67⁺ and RFP⁺ basal progenitors at E15.5. Error bars indicate SEM. *P < 0.05. (D to F) Coronal sections of two independent E18.5 mouse telencephali in utero electroporated at E13.5 with *ARHGAP11B* and GFP expression plasmids. (D and E) Phase contrast and GFP fluorescence in two consecutive sections along the rostro-caudal axis. Scale bars, 500 μm. (E) Electroporated area. Green and white dashed lines and triangles indicate gyrus- and sulcus-like structures in and adjacent to the electroporated area, respectively. (F) Satb2, NeuN, and Ctip2 immunofluorescence combined with DAPI staining and GFP immunofluorescence in two consecutive sections along the rostro-caudal axis. Scale bar, 250 μm. (G) Satb2 immunofluorescence of the cortical plate areas of the gyrus-like structure of *ARHGAP11B*-expressing neocortex located between white and green triangles in (F), and of the corresponding contralateral, control side. Scale bar, 50 μm.

in neocortex folding at E18.5, reminiscent of gyrification, a hallmark of human neocortex (Fig. 4). Cortical plate area in the gyrus-like structures was increased compared with the contralateral smooth neocortex, with proper cortical lamination.

The methodology for isolation of cortical progenitor subpopulations established here can be applied to other mammalian species, including primates, opening avenues for comparative evolutionary studies. Furthermore, the present transcriptome data provide insight into molecular differences between the various types of cortical NPCs in developing mouse and human neocortex and constitute a resource for future studies. A very recent, independent analysis of human radial glia transcriptome (*19*) has concentrated on genes present in both mouse and human genomes but expressed only in human cortical progenitors, identifying a role for platelet-derived growth factor signaling (*16*) in human radial glia. In contrast, we focus here on genes present only in the human, but not mouse, genome and highly expressed in basal radial glia.

Thus, we identify *ARHGAP11B* as a human-specific gene that amplifies basal progenitors and is capable of causing neocortex folding in mice (*33*, *34*). This probably reflects a role for ARHGAP11B in development and evolutionary expansion of the human neocortex, a conclusion consistent with the finding that the gene duplication that created *ARHGAP11B* occurred on the human lineage after the divergence from the chimpanzee lineage but before the divergence from Neandertals, whose brain size was similar to that of modern humans.

*Note added in proof*: In work published after online publication of this paper, Johnson *et al.* (*35*) used a complementary approach to similarly isolate and compare the transcriptomes of human and mouse apical and basal radial glia.

### REFERENCES AND NOTES

1. G. F. Striedter, *Principles of Brain Evolution* (Sinauer Associates, Sunderland, MA, 2005).
2. P. Rakic, *Nat. Rev. Neurosci.* **10**, 724–735 (2009).
3. J. H. Lui, D. V. Hansen, A. R. Kriegstein, *Cell* **146**, 18–36 (2011).
4. V. Borrell, I. Reillo, *Dev. Neurobiol.* **72**, 955–971 (2012).
5. M. Betizeau *et al.*, *Neuron* **80**, 442–457 (2013).
6. M. Florio, W. B. Huttner, *Development* **141**, 2182–2194 (2014).
7. V. Borrell, M. Götz, *Curr. Opin. Neurobiol.* **27**, 39–46 (2014).
8. T. Sun, R. F. Hevner, *Nat. Rev. Neurosci.* **15**, 217–232 (2014).
9. E. Taverna, M. Götz, W. B. Huttner, *Annu. Rev. Cell Dev. Biol.* **30**, 465–502 (2014).
10. I. H. Smart, C. Dehay, P. Giroud, M. Berland, H. Kennedy, *Cereb. Cortex* **12**, 37–53 (2002).
11. E. Lewitus, I. Kelava, A. T. Kalinka, P. Tomancak, W. B. Huttner, *PLOS Biol.* **12**, e1002000 (2014).
12. A. E. Ayoub *et al.*, *Proc. Natl. Acad. Sci. U.S.A.* **108**, 14950–14955 (2011).
13. S. A. Fietz *et al.*, *Proc. Natl. Acad. Sci. U.S.A.* **109**, 11836–11841 (2012).
14. M. L. Arcila *et al.*, *Neuron* **81**, 1255–1262 (2014).
15. J. A. Miller *et al.*, *Nature* **508**, 199–206 (2014).
16. Y. Arai *et al.*, *Nat. Commun.* **2**, 154 (2011).
17. A. Kawaguchi *et al.*, *Development* **135**, 3113–3124 (2008).
18. A. A. Pollen *et al.*, *Nat. Biotechnol.* **32**, 1053–1058 (2014).
19. J. H. Lui *et al.*, *Nature* **515**, 264–268 (2014).
20. S. A. Fietz, W. B. Huttner, *Curr. Opin. Neurobiol.* **21**, 23–35 (2011).
21. A. Attardo, F. Calegari, W. Haubensak, M. Wilsch-Bräuninger, W. B. Huttner, *PLOS ONE* **3**, e2388 (2008).
22. S. L. Houlihan, Y. Feng, *eLife* **3**, e03297 (2014).
23. A. Lukaszewicz *et al.*, *Neuron* **47**, 353–364 (2005).
24. X. Wang, J. W. Tsai, B. LaMonica, A. R. Kriegstein, *Nat. Neurosci.* **14**, 555–561 (2011).
25. B. Riley, M. Williamson, D. Collier, H. Wilkie, A. Makoff, *Genomics* **79**, 197–209 (2002).
26. F. Antonacci *et al.*, *Nat. Genet.* **46**, 1293–1302 (2014).
27. Y. Kagawa *et al.*, *PLOS ONE* **8**, e83629 (2013).
28. E. Zanin *et al.*, *Dev. Cell* **26**, 496–510 (2013).
29. P. H. Sudmant *et al.*, *Science* **330**, 641–646 (2010).
30. M. Meyer *et al.*, *Science* **338**, 222–226 (2012).
31. K. Prüfer *et al.*, *Nature* **505**, 43–49 (2014).
32. E. Taverna, C. Haffner, R. Pepperkok, W. B. Huttner, *Nat. Neurosci.* **15**, 329–337 (2012).
33. R. Stahl *et al.*, *Cell* **153**, 535–549 (2013).
34. B. G. Rash, S. Tomasi, H. D. Lim, C. Y. Suh, F. M. Vaccarino, *J. Neurosci.* **33**, 10802–10814 (2013).
35. M. B. Johnson *et al.*, *Nat. Neurosci.* 10.1038/nn.3980 (2015).

---

**PARASITOLOGY**

# The in vivo dynamics of antigenic variation in *Trypanosoma brucei*

Monica R. Mugnier, George A. M. Cross, F. Nina Papavasiliou*

*Trypanosoma brucei,* a causative agent of African Sleeping Sickness, constantly changes its dense variant surface glycoprotein (VSG) coat to avoid elimination by the immune system of its mammalian host, using an extensive repertoire of dedicated genes. However, the dynamics of VSG expression in *T. brucei* during an infection are poorly understood. We have developed a method, based on de novo assembly of VSGs, for quantitatively examining the diversity of expressed VSGs in any population of trypanosomes and monitored VSG population dynamics in vivo. Our experiments revealed unexpected diversity within parasite populations and a mechanism for diversifying the genome-encoded VSG repertoire. The interaction between *T. brucei* and its host is substantially more dynamic and nuanced than previously expected.

The protozoan parasite *Trypanosoma brucei*, a major cause of human and animal Trypanosomiasis, lives extracellularly within its mammalian host, where it is constantly exposed to the host immune system. *T. brucei* has evolved a mechanism for antigenic variation during infection in which the parasite can turn on and off variant surface glycoprotein (VSG)–encoding genes from a genomic repertoire of ~2000 different genes (*1*). Each parasite expresses one VSG at a time, from one of ~15 telomeric expression sites (*2*); the rest (silent VSGs) sit in silent expression sites or in other genomic locations (*1*). The highly antigenic VSG is so densely packed on *T. brucei's* surface that it obscures other cell-surface components from immune recognition. At any time, a few parasites in a population will stochastically switch their VSG. As previous variants are recognized by the immune system and cleared, newly switched variants emerge, giving rise to characteristic waves of parasitemia (*3*). These waves have long been interpreted as the sequential expression and clearance of one or a few VSGs, a notion supported by experimental evidence that relied on low-resolution approaches (*4*–*8*).

Despite attempts at modeling, little is known about the kinetics of VSG expression during infection (*9*–*12*). To assess this, we developed a targeted RNA sequencing (RNA-seq) approach, termed VSG-seq, in which VSG cDNA, amplified by using conserved sequences at the 5′ and 3′ end of every mature VSG mRNA (fig. S1), is sequenced and then assembled de novo by a transcriptome reconstruction method called Trinity (*13*). We validated

¹Laboratory of Lymphocyte Biology, The Rockefeller University, New York, NY, USA. ²Laboratory of Molecular Parasitology, The Rockefeller University, New York, NY, USA.
*Corresponding author. E-mail: papavasiliou@rockefeller.edu

**Human-specific gene *ARHGAP11B* promotes basal progenitor amplification and neocortex expansion**

Marta Florio *et al.*

*Science* **347**, 1465 (2015);
DOI: 10.1126/science.aaa1975